

Numerical Simulation for Three Dimensional Elastic-Plastic Contact With Hardening Behavior

Fan Wang

e-mail: fanwang@northwestern.edu

Leon M. Keer

Fellow

Center for Surface Engineering and Tribology,
Northwestern University,
2145 Sheridan Road,
Evanston, IL, 60208

An elastic-plastic contact (EPC) solution and code is developed using a modified semi-analytical method. The indentation tests with different hardening behavior are simulated by using the developed EPC code. The distributions of contact pressure, residual stress and plastic strain are obtained and compared with the results of the finite element method models without hardening. Some techniques, such as fast Fourier transform and fast convergence method, are used to increase the computation speed. [DOI: 10.1115/1.1924573]

Keywords: Elastic-Plastic, Contact, FFT, Residual Stress, Plastic Strain, Hardening Law

1 Introduction

One of the major forces applied to solid bodies is the contact force, which occurs when the bodies are brought together. The contact pressure and area are important parameters in understanding tribological phenomena, such as contact fatigue, wear and damage. When the surface geometry and the material properties are complicated, these parameters are not easily obtained.

Contact analysis can be traced back to 1882, in which Hertz studied the elastic contact between two glass lenses. Hertz theory is restricted to the normal frictionless contact between elastic half-spaces with small deformation.

Since then the modeling of contact has developed along two directions: stochastic approach and numerical modeling. The stochastic approach developed from work of Greenwood and Williamson [1], who pointed out that the surface asperity heights can be regarded as a Gaussian process and the contact on rough surfaces can be analyzed by using statistical methods. Other contributions include Refs. [2–6]. This theory was extended to non-Gaussian random process models by Bush et al. [7,8] and Suratkar et al. [9], and plasticity was also incorporated in Refs. [10–12]. However, the statistical approach cannot calculate the detailed values and distributions of contact area, pressure and stresses, which are the key points for the prediction of contact fatigue and wear. Numerical methods have been used to simulate contact problems for many years. They can be divided into the finite element analysis (FEA) and the semi-analytical method (SAM). The FEA, used in Refs. [13–17], can simulate complicated material behavior of contact bodies, but causes a time penalty if the surface is not smooth. Since the entire bulk of the contact body has to be modeled, the size of the elements near the rough surface should be very small. Many researchers use the SAM to analyze contact problems [18–21]. When using SAM, only a very small contact region needs to be considered, from which displacements are calculated based on the direct relationship between the contact pressure and contact displacement. Thus SAM is much faster than the finite element method (FEM), especially for three-dimensional (3D) contact. The fast Fourier transform (FFT) has been applied in SAM to further improve the speed of computation [22–26]. However, elastic or elastic-perfectly plastic material behavior is assumed in these works, which is not satisfied for materials with hardening behavior under mild pressure.

A modified SAM method is developed to simulate 3D elastic-

plastic contact in this paper. The approach is based on the work of Jacq et al. [27] and Mayeur et al. [28]. Purely elastic contact is calculated first. Next the distribution and value of plastic strain is determined using von Mises yield criterion and a specific hardening law. Finally the influence of the plastic deformation on the contact is considered, and the results of elastic contact are modified. Through simulation, the development of area and magnitude of the residual stress and plastic strain in the bodies along the loading process are accurately predicted. This approach can simulate elastic-plastic contact with different hardening behavior, which is an advantage compared to other SAM methods. Some techniques, such as FFT and fast convergence method (FCM), are applied to increase the speed of computation.

2 Elastic Contact

The geometry of a typical contact problem is shown in Fig. 1, where ω is the relative approach. If there is no deformation in the bodies, the surfaces will overlap as shown in the dashed line. Since the bodies cannot interpenetrate each other, deformation is necessary. The displacements of the contact surfaces are u_1 and u_2 . The gap between the surfaces, h , can be expressed as

$$h = h_i + (u_1 + u_2) - \omega \quad (1)$$

where h_i is the initial gap without loading. If the point is inside the contact region, the gap equals zero; otherwise it is larger than zero. The contact pressure p is positive inside the contact region and zero outside the contact region. Thus the contact region is determined by inequalities, which are expressed below:

Inside the contact region: $h = 0$ and $p \geq 0$

Outside the contact region: $h > 0$ and $p = 0$ (2)

At the contact surface the loading and pressure distribution has to satisfy an equilibrium equation

$$L = \int_{\Gamma_c} p(x_1, x_2) d\Gamma \quad (3)$$

where L is the external load. Other elasticity equations include the following:

$$\text{Strain-displacement relations: } \varepsilon_{ij} = \frac{1}{2}(u_{i,j} + u_{j,i}) \quad (4)$$

$$\text{Equilibrium equation: } \sigma_{ij,j} = 0 \quad (5)$$

Contributed by the Tribology Division for publication in the ASME JOURNAL OF TRIBOLOGY. Manuscript received June 23, 2004; final manuscript received March 24, 2005. Review conducted by: Michael Lovell.

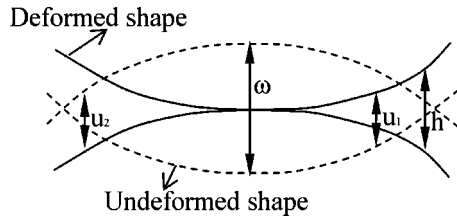


Fig. 1 Typical contact problem

$$\text{Hooke's law: } \sigma_{ij} = 2\mu \left(\varepsilon_{ij} + \frac{\nu}{1-2\nu} \delta_{ij} \varepsilon_{kk} \right) \quad (6)$$

The theoretical approach for elastic contact on the half-space was developed by Boussinesq [29] and Cerruti [30] using potential theory, which was presented in Ref. [18]. Boussinesq developed the relationship between the concentrated point force P and the normal surface deflection u_z as

$$u_z = \frac{1-\nu^2}{\pi E} \frac{P}{r} \quad (7)$$

where r is the distance from the reference point to the loading point. The surface displacement is the sum of the u_z induced by the loading on each point of the contact region S . The expressions for surface displacement are shown in Eqs. (8) and (9) [31]:

$$u_z = \frac{1-\nu^2}{\pi E^*} \int p(s) \ln \left(\frac{x-s}{x_r-s} \right)^2 ds \quad (2D) \quad (8)$$

$$u(x,y) = \frac{1-\nu^2}{\pi E^*} \iint_{\Omega} \frac{p(x',y') dx' dy'}{\sqrt{(x-x')^2 + (y-y')^2}} \quad (3D) \quad (9)$$

where E^* is the composite Young's modulus, defined as

$$\frac{1}{E^*} = \frac{1-\nu_1^2}{E_1} + \frac{1-\nu_2^2}{E_2} \quad (10)$$

To calculate the integral, a grid system was used (see Fig. 2). The potential contact surface is divided into many similar rectangular elements with size $2a \times 2b$. The contact pressure is assumed to be constant for each element. The total deflection at the reference point (i,j) is the sum of $K_{|i-k|,|j-\ell|}$ times the magnitude value of the element pressure $p_{k\ell}$ at the point (k,ℓ) [32]. The influence coefficient $K_{|i-k|,|j-\ell|}$ is the integral value of deflection at point (i,j) induced by each unit element pressure $\bar{p}_{k,\ell}$. The set of the total grid nodes is I_g , and the set of the nodes in contact is I_c .

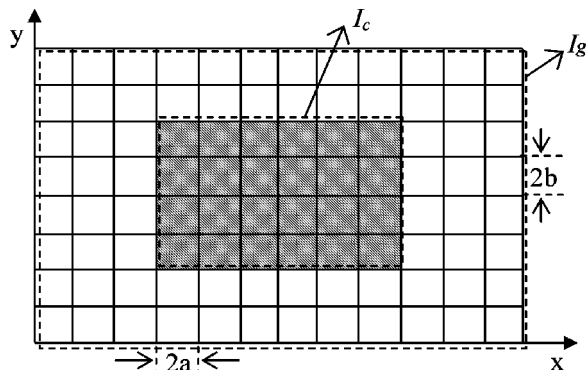


Fig. 2 Grid system of the contact surface

$$u_{ij} = - \sum_{(k,\ell) \in I_g} K_{|i-k|,|j-\ell|} p_{k\ell} \quad (i,j) \in I_g \quad (11)$$

For the contact problem, the external load L is specified, while the approach ω , contact region I_c , and contact pressure p_{ij} are unknown. An iterative scheme based on the conjugate gradient method [33–35] is used to solve this problem.

The subsurface stress in the contact solid can be calculated after the contact pressure p_{ij} is obtained. The formula is shown as Eq. (12) [21].

$$\sigma_{mn}(x_i, y_i, z) = \sum_{(k,\ell) \in I_g} [S_{i-k,j-\ell}^{mn}(z) + \tau T_{i-k,j-\ell}^{mn}(z)] p_{k\ell}, \quad m, n = 1, 2, 3, \quad (i,j) \in I_g \quad (12)$$

where τ is the coefficient of friction, and $S_{ij}^{mn}(z)$ and $T_{ij}^{mn}(z)$ are, respectively, the stress influence coefficients for the normal and tangential contact loading. Their detailed expressions can be found in Ref. [36].

In Eq. (11), the deflection at a reference node is the sum of the deflections produced by each element pressure. Thus $O(N)$ multiplication operations are needed to calculate the node deflection, if the total elements in the grid system is N . In order to obtain the deflection at all over the nodes in the contact surface $O(N^2)$ operations are required. This process is called direct multisummation and is costly in computation time if N is a large number. This shortcoming can be overcome through using a FFT technique.

The Fourier transform (FT) can transfer a space variable domain into the frequency domain. The discrete two-dimensional (2D) FT is defined as follows:

$$\hat{p}_{k\ell} = \sum_{m=0}^{M_x-1} \sum_{n=0}^{M_y-1} e^{i2\pi mk/N_x} e^{i2\pi n\ell/N_y} p_{mn}, \quad (k,\ell) \in I_g \quad (13)$$

Since Eq. (11) is a discrete convolution of K_{ij} with p_{ij} and a convolution operation in the space domain can be replaced by a multiplication operation in the frequency domain [23], the following equation yields

$$\hat{u}_{ij} = - \hat{K}_{ij} \hat{p}_{ij}, \quad (i,j) \in I_g \quad (14)$$

where \hat{u}_{ij} and \hat{K}_{ij} are the Fourier transforms of u_{ij} and K_{ij} separately. The finally nodal deflection u_{ij} is obtained through an inverse FT performed on \hat{u}_{ij} .

There are $O(N)$ operations required in Eq. (14), but a FFT technique is used instead of FT, which can reduce the operations to $O(\log N)$. Thus $O(N \log N)$ operations are needed to obtain \hat{u}_{ij} at all the nodes on the surface. A detailed description of this technique can be found in Ref. [37].

The FFT can also be applied in Eq. (12) to calculate contact stress field, which is introduced in [38].

3 Elastic-Plastic Contact

3.1 Introduction. The analytical approach for elastic contact has been introduced in the former section, but it cannot be used for inelastic conditions. For example, when bodies with rough surfaces are in contact under a heavy load, a concentrated stress will occur at or near the rough surfaces. The magnitude of stress is sometimes much higher than the yield strength of the material, and plastic deformation will occur. Elastic-plastic contact is more complicated than purely elastic contact, since the magnitude and distribution of plastic deformation must be determined.

It is found that the development of the plastic strain with the loading process can be divided into three ranges [32]: I Purely elastic, II Elastic-plastic, and III Perfectly plastic (see Fig. 3). Suppose the loading is applied gradually from zero to a high value. In range I, there is no plastic deformations, and the stress fields in the body increase with the loading until they reach the yield strength. In range II, the yield point is exceeded, and a

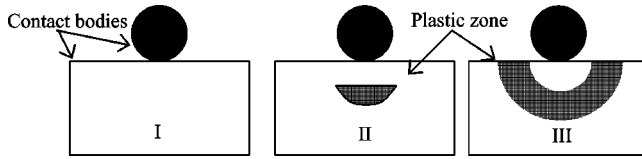


Fig. 3 The three ranges for the development of plastic zone

plastic zone develops, which is too small to reach the surface. There is a plastic core surrounded by an elastic region, and the plastic strain is the same order of magnitude as the surrounding elastic strain. In the third range, the plastic zone reaches the free surface and the displaced material can easily escape by plastic flow to the side of the indenter.

The three ranges have different behavior for plastic deformation, and they respond to different stress-strain relationships as follows (see Fig. 4):

Range I: Purely elastic (1)

Range II: Elastic-plastic (3) or (4)

Range III: Fully plastic (2)

In Refs. [21,24] the material is restricted in elastic or elastic-perfectly plastic. Thus the plastic zone develops directly from range I to range III without achieving the middle range. This case corresponds to the heavy loading. If the load is not very large or the rate of loading is small, the plastic zone will expand gradually and range II also becomes important. This paper is focused on the elastic-plastic contact. The development of the plastic strain zone during range II is simulated by modeling of the hardening law.

3.2 Basic Formulas for Elastic-Plastic Contact. For elastic-plastic contact, the normal deflection is not only induced by the contact pressure, but also depends on the plastic strain (see Fig. 5). It is expressed in Eq. (15).

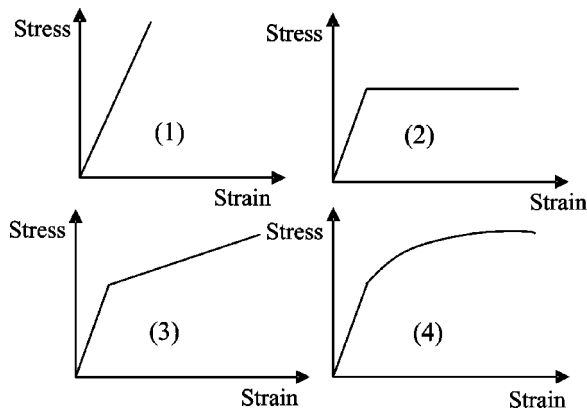


Fig. 4 Stress strain relationships, (1) pure elastic, (2) elastic-perfect plastic, (3) linear hardening, and (4) power law hardening

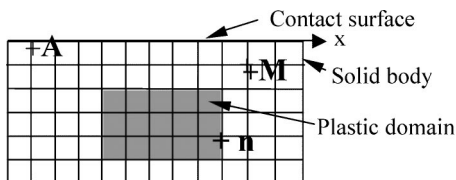


Fig. 5 Grid system of the contact body in x - z section

$$u_{k(\text{total})} = \int_{\Gamma_c} u_i^*[M, p^*(A)] p_i(M) d\Gamma + 2\mu \int_{\Omega_p} \varepsilon_{ij}^p(M) \varepsilon_{ij}^*[M, p^*(A)] d\Omega \quad k = 1, 2, 3 \quad (15)$$

A reciprocal theorem was used to derive this formula. Suppose two independent loads are applied to an elastic body with volume Ω and boundary Γ . The first state (u, ε, σ) exists with an initial plastic strain ε^p , and the second state $(u^*, \varepsilon^*, \sigma^*)$ corresponds to the application of a unit force along k ($k=1, 2, 3$) direction at point A . A point M is in the integration surface or volume, Γ_c is the boundary of the contact region, Ω_p is the volume of the plastic strain, and μ is the shear modulus. The detailed derivation can be found in Refs. [27,39]. Let

$$u_{k(\text{pressure})} = \int_{\Gamma_c} u_i^*[M, p^*(A)] p_i(M) d\Gamma \quad k = 1, 2, 3 \quad (16)$$

$$u_{k(r)} = 2\mu \int_{\Omega_p} \varepsilon_{ij}^p(M) \varepsilon_{ij}^*[M, p^*(A)] d\Omega \quad k = 1, 2, 3 \quad (17)$$

therefore

$$u_{k(\text{total})} = u_{k(\text{pressure})} + u_{k(r)} \quad (18)$$

Hooke's law is given as

$$\begin{aligned} \sigma_{\text{total}} &= \mathbf{C} : \varepsilon_e = \mathbf{C} : (\varepsilon_{\text{total}} - \varepsilon_p) = \mathbf{C} : (\varepsilon_{\text{pressure}} + \varepsilon_r - \varepsilon_p) \\ &= \mathbf{C} : \varepsilon_{\text{pressure}} + \mathbf{C} : (\varepsilon_r - \varepsilon_p) \end{aligned} \quad (19)$$

where \mathbf{C} is the tensor for elastic moduli, and

$$\varepsilon_{ij(r)} = \frac{1}{2} (u_{i,j(r)} + u_{j,i(r)}) \quad (20)$$

Let

$$\sigma_{\text{pressure}} = \mathbf{C} : \varepsilon_{\text{pressure}}, \quad \sigma_r = \mathbf{C} : (\varepsilon_r - \varepsilon_p) \quad (21)$$

then Eq. (19) becomes

$$\sigma_{\text{total}} = \sigma_{\text{pressure}} + \sigma_r \quad (22)$$

Here σ_{pressure} is the stress due to contact pressure, and σ_r is the residual stress which is linked to the plastic strain and remains after unloading.

The definition of u_r is given in Eq. (17), and since it is related to plastic strain, u_r is called the residual displacement. The domain of plastic strain is divided into N_v cubic elements with equal volume Ω_p . The plastic strain in each cube is assumed constant. Thus the residual displacement can be seen as the sum of the integral at each cube

$$u_{3(r)}(A) = 2\mu \sum_{n=1}^{N_v} \varepsilon_{ij}^p(n) \int_{\Omega_{cn}} \varepsilon_{ij}^*[M, p^*(A)] d\Omega = \sum_{n=1}^{N_v} \varepsilon_{ij}^p(n) D_{ij}(n) \quad (23)$$

with

$$D_{ij} = 2\mu \int_{\Omega_{cn}} \varepsilon_{ij}^* d\Omega \quad (24)$$

Here ε_{ij}^* is the strain state linked to the application of a unit force along x_3 direction at point A . The detailed expression of D_{ij} can be found in Refs. [18,27].

The residual stress σ_r is the stress field produced by a plastic strain zone in a half-space with a free surface. In order to calculate the integral the plastic strain volume is also divided into N_v cubic elements. The residual stress at a reference point M induced by a cubic plastic element n can be expressed as:

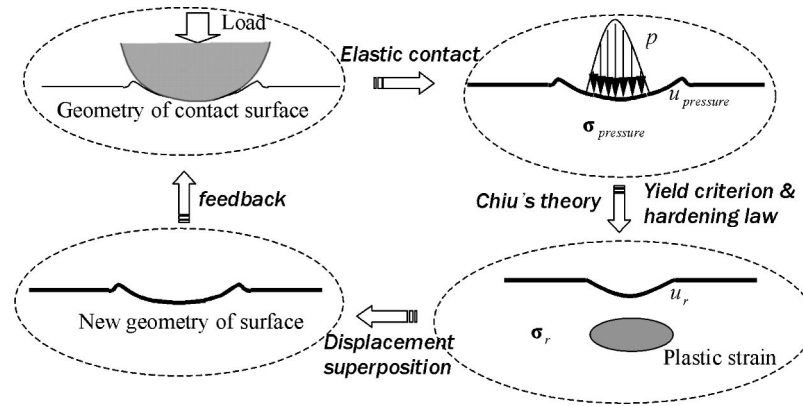


Fig. 6 Resolving process of elastic-plastic contact

$$\sigma_{ij(r)}(M) = \sum_{n=1}^{N_v} A_{ijk\ell}(M, n) \varepsilon_{k\ell}^p(n) \quad (25)$$

The detailed description of $A_{ijk\ell}$ is in Refs. [40,41].

3.3 Resolving Process for Elastic-Plastic Contact. Equation (18) shows that the total displacement of the points on the surface is the sum of residual displacement u_r and the displacement produced by the contact pressure u_{pressure} , which can be calculated by using an iterative method. Purely elastic contact is calculated first and based on the work of Polonsky et al. [21] and Liu et al. [24]. The pressure distribution p , stress field σ_{pressure} , and surface displacement u_{pressure} are obtained using the method introduced in Sec. 2. The plastic strain distribution is calculated using a yield criterion and hardening law. The displacement due to plastic strain u_r is calculated next. Since u_r changes the shape of the surface, the elastic contact has to be recalculated based on the new surface geometry. The calculation is repeated until convergence occurs. The computation process is shown as Fig. 6; the code description based on this process is given in the Appendix.

3.4 Methods to Increase the Speed of Computation.

3.4.1 Fast Fourier Transform. The FFT is applied in the calculation of surface deflection to increase the speed of computation, which was introduced in Sec. 2. In the calculation of residual stress, multisummation has to be performed in a 3D domain and has a greater time penalty than in the deflection calculation. The FFT technique is used to resolve this problem. Equation (25) can be rewritten as follows:

$$\sigma_{pq(r)}(x_i, y_j, z_k) = \sum_{n=1}^{N_z} \sum_{\ell=1}^{N_x} \sum_{m=1}^{N_y} A_{pqrs}^{[i-\ell, |j-m|, |k-n|]}(z_n) \varepsilon_{rs}^{\ell, m, n(p)}, \quad (26)$$

$1 \leq i \leq N_x, \quad 1 \leq j \leq N_y, \quad 1 \leq k \leq N_z, \quad p, q, r, s = 1, 2, 3.$

Here N_x, N_y, N_z are the limit numbers of the grid system in the x, y , and z direction. The influence coefficient $A_{pqrs}^{[i-\ell, |j-m|, |k-n|]}(z_n)$ is related to z_n , which is the coordinate in z direction of the plastic element. Thus FFT cannot be used directly in Eq. (26). The 2D multisummation in a particular x - y plane ($z = z_n$) is expressed as follows:

$$\sigma_{\text{sum}}^{i,j}(z_k, z_n) = \sum_{\ell=1}^{N_x} \sum_{m=1}^{N_y} A^{[i-\ell, |j-m|]}(z_k, z_n) \varepsilon^{\ell, m(p)}(z_n) \quad (27)$$

The residual stress is the sum of $\sigma_{\text{sum}}^{i,j}(z_k, z_n)$ in all x - y planes.

$$\sigma_r(x_i, y_j, z_k) = \sum_{n=1}^{N_z} \sigma_{\text{sum}}^{i,j}(z_k, z_n) \quad (28)$$

Based on the convolution theorem, the FFT can be applied in Eq. (27), and yields the following equation:

$$\hat{\sigma}_{\text{sum}}^{i,j}(z_k, z_n) = \hat{A}^{i,j}(z_k, z_n) \hat{\varepsilon}^{i,j(p)}(z_n), \quad 1 \leq i \leq N_x, \quad 1 \leq j \leq N_y \quad (29)$$

Without using FFT, $O(N_x^2 N_y^2 N_z^2)$ mathematical operations are required to obtain the residual stress at all the nodes of the body. This number decreases to $O(N_z^2 N_x N_y \log N_x \log N_y)$ if FFT is used.

3.4.2 Fast Convergence Method. As the last section stated, the residual stress calculation is a multilevel multiplication in 3D body and consumes considerable computation time. This calculation must be performed many times for each loading step. There are two nested loops in each loading step: the elastic-plastic loop (E loop) and the plastic strain loop (P loop). The residual stress calculation is inside the P loop, which is inside the E loop (see Appendix). Suppose the loop number for the E loop and P loop are S and T , separately in a given loading step. The residual stress has to be calculated $S \times T$ times for this step, which accounts for the major portion of the total computation time. Therefore the convergence speeds of the E loop and P loop are the key point for determining the final calculation speed. The E loop and P loop converge well when the load is small, but the convergences become difficult when the load is large, because of the influence of plastic deformation. The difficulty can be overcome by using the FCM technique.

In the EPC code the E loop and P loop computations are performed to get the accurate values for residual displacement increment δu^r and plastic strain increment $\delta \varepsilon^p$ separately. Since neither δu^r nor $\delta \varepsilon^p$ has an explicit solution, an iteration method is applied. First an initial estimate of δu^r or $\delta \varepsilon^p$ is set at the beginning of E loop or P loop. The next value of δu^r or $\delta \varepsilon^p$ is then calculated based on the value of the last loop step. The iterative calculation is continued until the convergence conditions are satisfied. Although the initial value is usually set as zero for iterative problems, through a computation test zero is not found to be an economic initial value for EPC contact with high plastic deformation because it leads to too many loop steps for the E loop and P loop. For two successive loading steps δu^r are quite similar if the loading step length is not very large. Therefore, the initial value of δu^r can be set as the value achieved at the last loading step. Also, $\delta \varepsilon^p$ for two successive E loop steps are similar, and the initial value of $\delta \varepsilon^p$ is supposed to be the value of last E loop step. Through these nonzero-initial-value settings, the iterative calculation of last loading step or E loop step can be contributed to the calculation of

Table 1 Convergence speed comparison between EPC code and Jacq's code

	Average loop number for E loop	Average loop number for P loop	Total P loop number for each loading step
EPC code with FCM	3	7	21
Jacq's code[27]	10	80-5	300

current step and the process converges much more rapidly (See Table 1). The detailed FCM settings are as follows:

If $k = 1$, initial $\delta u_k^r = 0$; If $k > 1$, initial $\delta u_k^r = \delta u_{k-1}^r$

If $i = 1$, initial $\delta \epsilon_i^p = f(\sigma_{\text{pressure}}, \sigma_r, \delta \sigma_{\text{pressure}})$; (30)

If $i > 1$, initial $\delta \epsilon_i^p = \delta \epsilon_{i-1}^p$

where k is the current loading step number and i is the current step number of E loop.

The computational test shows that the FCM technique leads to rapid convergence for the E loop and P loop and has a huge computational advantage compared to the code without FCM [27] (see Table 1).

4 Calculation Examples–3D Numerical Simulation of Indentation of Steel

4.1 Introduction of the Computation Example. A 3D numerical simulation is performed for an indentation test (see Fig. 7). Using the EPC code. The punch and the indentation substrate are simplified as a spherical rigid body and a steel half-space separately. Smooth surfaces are assumed for both the punch and the half-space. The geometry and material properties are listed in Table 2. Two groups of material parameters are used in the simulation. Here ν is Poisson's ratio; σ_{Y0} , E and E_T are parameters for linear hardening law; B , C , and n are constants for Swift's hardening law. The detailed introduction of these parameters is in the next section.

4.2 Plastic Modeling. The von Mises yield criterion is applied here, since it is well suited to steel, and is given as follows:

$$f = \sigma_{VM} - \sigma_Y = \sqrt{\frac{3}{2} S_{kl} : S_{kl}} - \sigma_Y \quad (31)$$

where σ_Y is the yield strength, σ_{VM} is the von Mises stress, and $S_{kl} = \sigma_{kl} - 1/3 \sigma_{ii} \delta_{kl}$. Using the Prandtl–Reuss equation the plastic strain rate can be calculated:

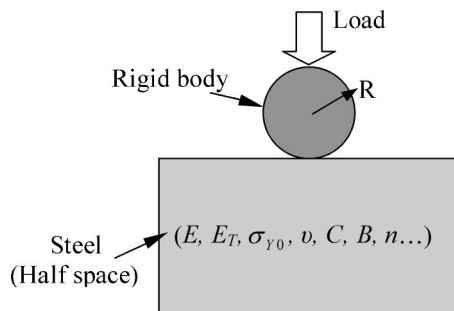


Fig. 7 Simplified indentation test

Table 2 Material constants of the steel body

Models	R (mm)	ν	E (GPa)	E_T (GPa)	σ_{Y0} (MPa)	B (MPa)	C	n
Swift's law	0.5	0.4	210	—	—	899 449	30	0.085
Linear hardening law	0.5	0.4	210	0.8E 0.5E	1200 600	—	—	—

$$d\epsilon_{ij}^p = \frac{3S_{ij}d\sigma_{VM}}{2\sigma_{VM}H'} \quad (32)$$

where H' is the slope of the curve of equivalent plastic strain versus equivalent stress, $d\epsilon^p$ is inverse proportion to H' . The lower value of slope leads to the larger plastic deformation increment. As the limit case, perfect plasticity has zero value of H' and causes Eq. (32) to be invalid since it leads to infinite plastic deformation. In this paper materials with plastic hardening behavior are studied and perfect plasticity is not considered. Experiments prove that this nonzero-slope assumption is suitable to most of steel and alloy materials.

In order to study the contact behavior for different hardening models, two kinds of hardening laws are simulated using EPC code: Swift's hardening law and linear hardening law.

For Swift's law (Fig. 8) H' has a high value at the beginning of the hardening curve, and then gradually decreases, which fits the character of bearing steel. Its expression is as follows:

$$\sigma_Y = B(C + \epsilon^p)^n \quad (33)$$

where B , C , and n are the constants of Swift's law, $\epsilon^p = \sqrt{2/3} \epsilon_{kl}^p : \epsilon_{kl}^p$.

The expression of H' for Swift's law is then derived from Eq. (33)

$$H' = Bn \left(\frac{\sigma_Y}{B} \right)^{1-1/n} \quad (34)$$

The plastic strain rate can be derived from Eqs. (32) and (34) as follows:

If $f \geq 0$, let $\sigma_Y = \sigma_{VM}$

$$d\epsilon_{ij}^p = \frac{3S_{ij}d\sigma_{VM}}{2Bn\sigma_{VM}} \left(\frac{\sigma_{VM}}{B} \right)^{1/n-1} \quad (35)$$

If $f < 0$, $d\epsilon_{ij}^p = 0$

The linear hardening law is also applied (Fig. 9), which is expressed as follows:

$$\sigma_Y = \sigma_{Y0} + \frac{E_T}{1 - E_T/E} \epsilon^p \quad (36)$$

where E is Young's modulus, E_T is the elastic-plastic tangential modulus, and σ_{Y0} is the initial yield stress.

For the linear hardening law H' is a constant and depends on the material parameters E and E_T :

$$H' = \frac{E_T}{1 - E_T/E} \quad (37)$$

The plastic strain rate has non-zero value if $f \geq 0$:

$$d\epsilon_{ij}^p = \frac{3S_{ij}d\sigma_{VM}(1 - E_T/E)}{2\sigma_{VM}E_T} \quad (38)$$

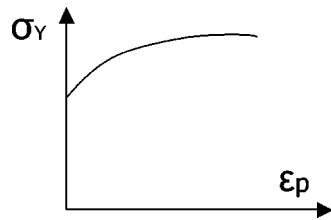


Fig. 8 Swift's hardening law

4.3 Results Analysis. Figure 10 shows the initial surfaces and deformed surfaces in the x - z section as an example of the results using Swift's hardening law. For the initial contact case, the external load is zero, and surface 1 contacts with surface 2 at a particular point ($x=0.062$ mm), where the gap between 1 and 2 is zero. At other locations the gap has a positive value. Since the indenter is rigid, the shape of surface 2 does not change as the load reaches 4730 mN, while surface 1 becomes a concave plane due to elastic and plastic deformation. The gap is zero inside the contact region, but larger than zero outside this region.

The corresponding contact pressure distribution along x is shown in Fig. 11. The maximum value is 3.25 GPa. Unlike the results for elastic contact, the pressure curve becomes flattened for elastic-plastic contact. The size of the non-zero pressure region is identical to the size of the contact region in Fig. 10. Thus the inequalities in Eq. (2) are satisfied.

The contact pressure curves for different hardening models are compared in Figs. 12 and 13, which correspond to different initial yield stress. The five hardening models are as follows: purely elastic, Swift's law, linear hardening with $E_T=0.8E$ (L0.8), linear hardening with $E_T=0.5E$ (L0.5), and a FEM model with perfect plasticity [14]. The dimensionless contact radius x/a_0 and dimensionless pressure p/p_0 are the abscissa and ordinate. Here p_0 and a_0 are maximum pressure and contact radius for purely elastic contact results.

The purely elastic model gives the maximum dimensionless pressure as 1. The figure shows the curve of Swift's law is flatter than the curve of L0.8, while the curve of L0.5 is flatter than the curve of Swift's law. The curve of L0.5 is near to the curve for the

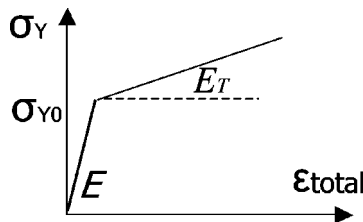


Fig. 9 Linear hardening law

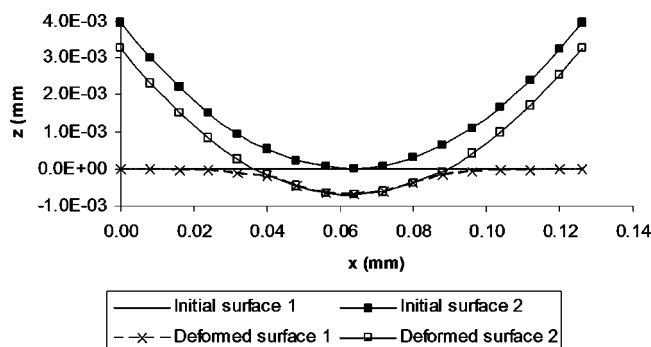


Fig. 10 Initial and deformed contact surfaces in x - z section

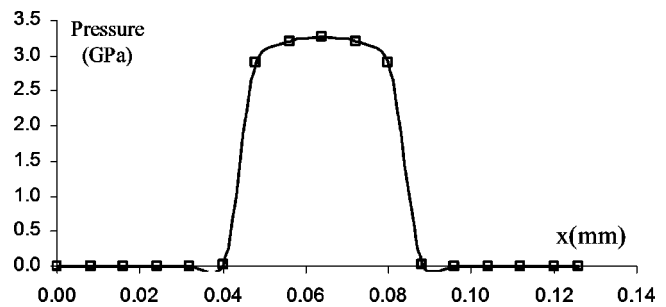


Fig. 11 Surface pressure distribution along x , load=4730 mN

perfectly plastic model. The larger E_T will lead to the flatter pressure curve. The peak stress p_0 is fixed at 2969 MPa for both cases, but the initial yield stress is decreased from 1200 MPa (Fig. 12) to 600 MPa (Fig. 13). Thus Fig. 13 shows the case with larger plastic deformation. In Fig. 13 the pressure curves for the hardening models are much flatter than the purely elastic model, but similar to the perfectly plastic model.

The curves of dimensionless contact approach versus dimensionless mean pressure for different hardening behavior are drawn in Fig. 14. In order to decrease the effects of geometry and yield stress, non-dimensional pressure p_m/σ_{Y0} and non-dimensional approach ω/ω_c are applied here. The critical contact approach ω_c , which is the approach at the transition point from the elastic to the elastic-plastic contact, is expressed as follows [15]:

$$\omega_c = \left(\frac{\pi K H}{2 E^*} \right)^2 R$$

where H is the hardness and depends on the yield stress as $H = 2.8\sigma_{Y0}$, K is related to the poisson's ratio as $K = 0.454 + 0.41\nu$, and E^* is defined in Eq. (10).

When the dimensionless pressure is less than 1.6 the curves are straight lines and have a similar slope of 0.22 except for the CEB

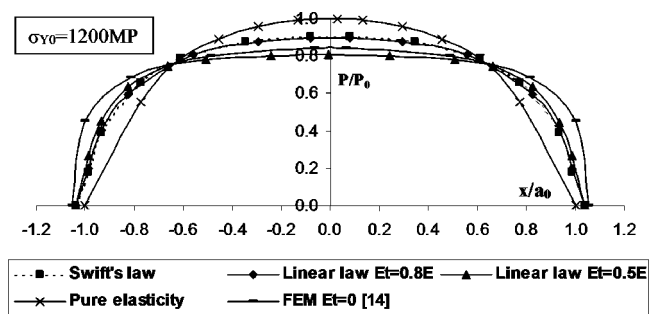


Fig. 12 Dimensionless contact radius versus dimensionless contact pressure for different material models, $\sigma_{Y0}=1200$ MPa

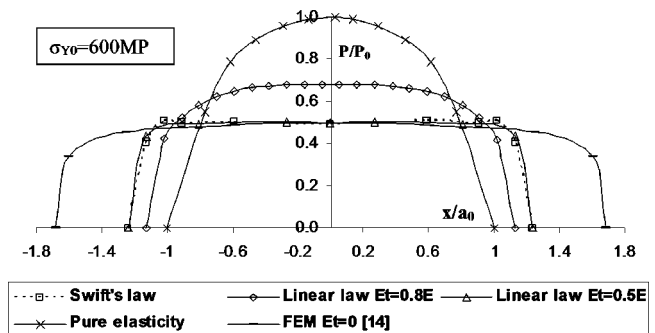


Fig. 13 Dimensionless contact radius versus dimensionless contact pressure for different material models, $\sigma_{Y0}=600$ MPa

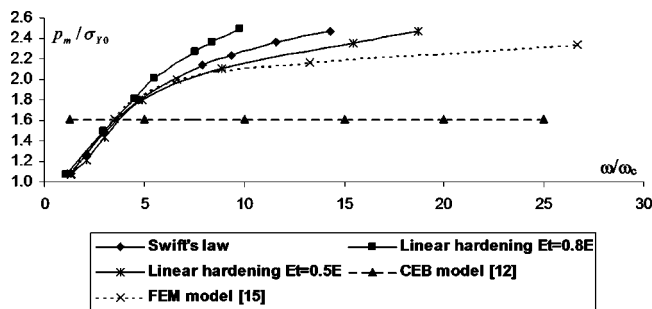


Fig. 14 Dimensionless approach ω/ω_c versus dimensionless mean pressure p_m/σ_{y0}

model by Chang et al. [12]. Thus the hardening effect on the elastic-plastic contact is small for small pressure case. When the dimensionless pressure is between 1.6 and 2.8 the curves are different for different models. The larger hardening behavior will lead to the smaller contact approach. If the dimensionless pressure is fixed at the same value, the order of the models with the approach from low to high is: L0.8, Swift's law, L0.5, FEM model with perfect plasticity [15], and CEB model. The slopes of the curves gradually decrease with increase of pressure. When the dimensionless pressure is larger than 2.8 the slopes are nearly zero, which leads to a much larger contact approach and includes the third contact stage: perfectly plastic contact.

Figures 15–18 show the results using Swift's hardening law. Figure 15 shows the distribution of von Mises stress in an x - z section when the load equals 530 and 4730 mN separately. Two non-dimensional values, x/a and z/a , are used separately for the x and y axis. Here a is the critical contact length as $a=(R\omega_c)^{1/2}$. The maximum von Mises stress occurs at some point beneath the contact surface, and the depth of the maximum stress increases with load increase. The maximum value increases from 1550 to 1850 MPa as the load increases.

Figure 16 shows the distribution of residual stress in the x - z section with two different loadings. The maximum value of residual stress also occurs at a location below the contact surface, and the depth of the maximum stress increases with an increase of the load. The residual stress is less than one-tenth of the von Mises stress, but quickly increases. The ratio of the maximum residual stress to the maximum von Mises stress increases from 3% to 10% as the load increases from 530 to 4730 mN.

Figure 17 shows the distribution of the residual displacement $u_{3(r)}$ along x . The maximum value (2.39×10^{-4} mm) occurs at the center of the contact region, and $u_{3(r)}$ has a high positive value at the center and smaller negative values away from the center. The final gap is thus made more uniform, and the pressure distribution

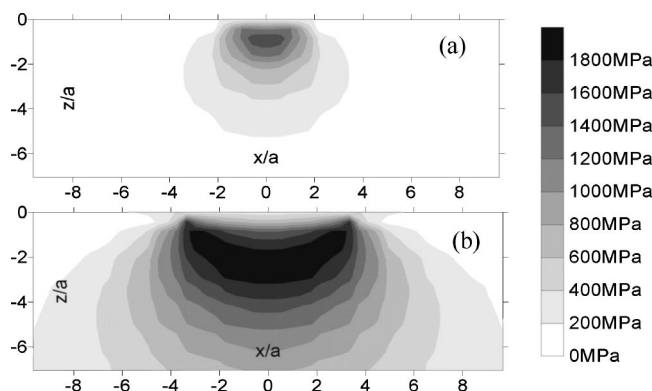


Fig. 15 Distribution of von Mises stress in x - z section, (a) load=530 mN, (b) load=4730 mN

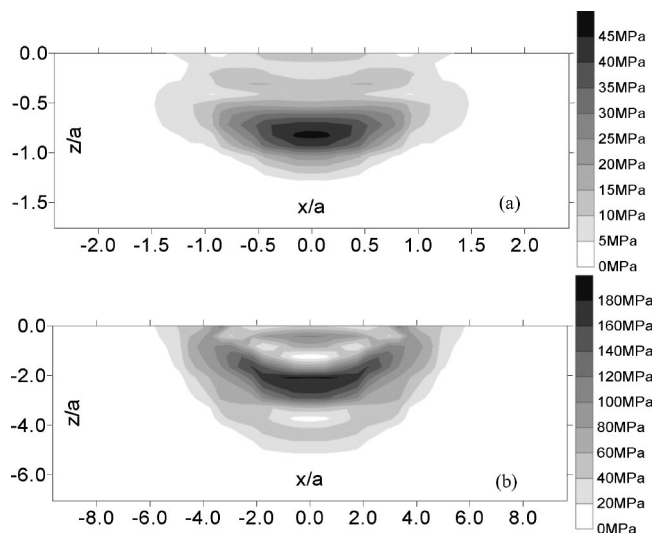


Fig. 16 Distribution of residual stress in x - z section, (a) load=530 mN, (b) load=4730 mN

is therefore flattened (see Figs. 12 and 13).

Figure 18 shows the distribution of equivalent plastic strain in x - z section at two different loadings. At low loading case the plastic region is a small half-ellipsoid and below the contact surface. The maximum plastic deformation is 0.05%. The plastic re-

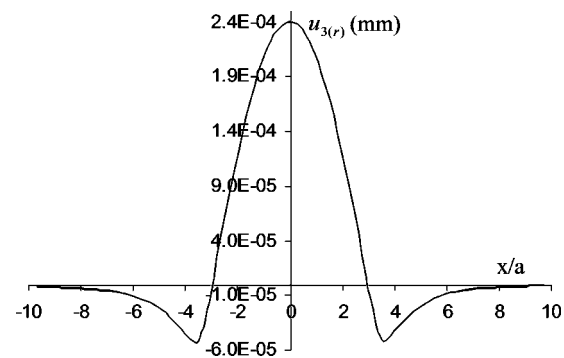


Fig. 17 Distribution of residual displacement $u_{3(r)}$ along x

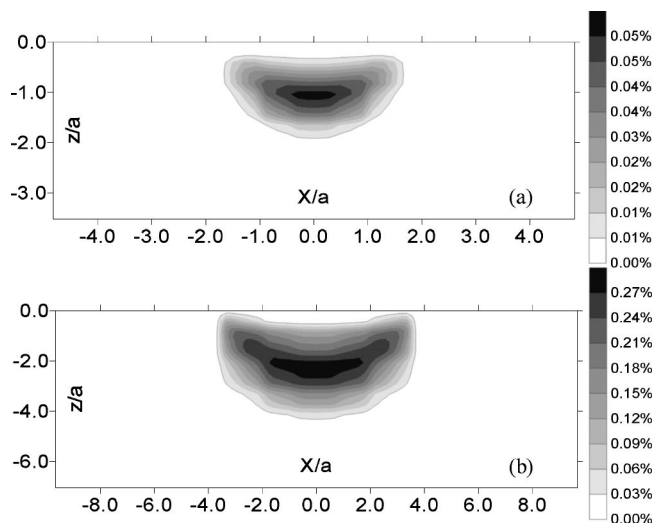


Fig. 18 Distribution of equivalent plastic strain in x - z section, (a) load=530 mN, (b) load=4730 mN

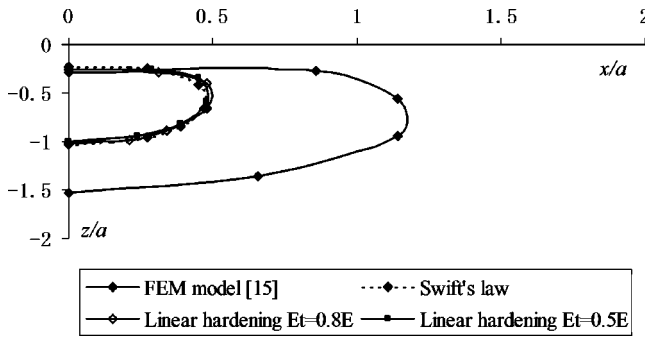


Fig. 19 Comparison of plastic region for different hardening behavior, $\omega/\omega_c=2$

gion gradually expands with an increase of load. At the high loading case the plastic region turns upwards and reaches the contact surface. There is an elastic core surrounded by the plastic region near the center of the contact region. The maximum plastic strain reaches a high value of 0.27% when load equals 4730 mN.

The development of a plastic region in the half x - z section with the increase of dimensionless approach ω/ω_c is shown in Figs. 19–21. In each figure there are four curves denoted by Swift's law, L0.5, L0.8, and FEM model with perfect plasticity [15]. When the dimensionless approach ω/ω_c is 2, the plastic deformation is small, the Swift's law, L0.5, and L0.8 have similar plastic regions. When ω/ω_c is 6, the plastic region reaches the contact surface, and there is an elastic core near the contact region surrounded by the plastic region. When ω/ω_c is 11, the plastic region is larger. The order of the plastic area for different models from small to large is: L0.8, Swift's law, L0.5, and FEM model. The plastic region for FEM model has the largest area because of the perfectly plastic assumption.

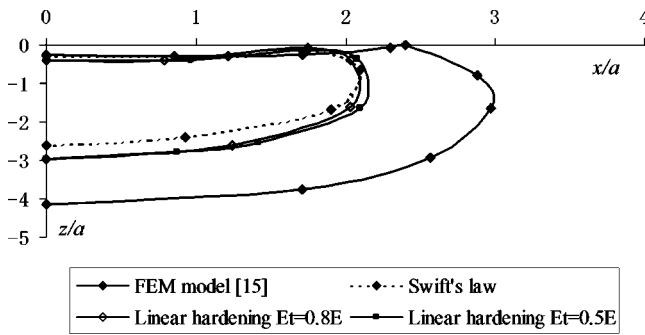


Fig. 20 Comparison of plastic region for different hardening behavior, $\omega/\omega_c=6$

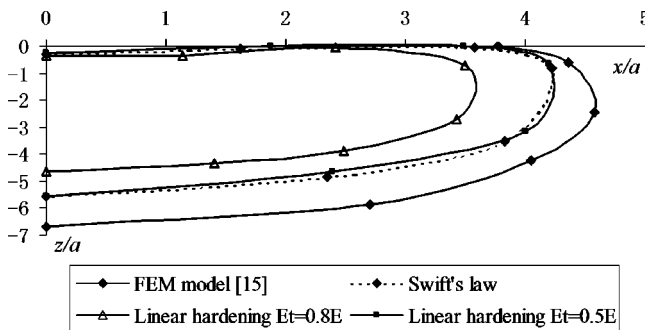


Fig. 21 Comparison of plastic region for different hardening behavior, $\omega/\omega_c=11$

5 Conclusion

This paper develops a code, which can simulate the 3D elastic-plastic contact. Since the total surface deflection is induced by the contact pressure and plastic strain, an iterative approach is used. The purely elastic contact and the influence of the plastic strain are calculated iteratively until convergence is satisfied. Through computation, the detailed distribution of residual stress and plastic strain within the contact body are obtained. The EPC code can simulate materials with different hardening behavior, which is an advantage over other SAM codes. FFT and FCM techniques are used to enhance the speed of computation. The indentation test is simulated using the developed EPC code. The distributions of von Mises stress, plastic strain and residual stress within the contact body are obtained. The pressure curves and plastic regions for different hardening models are compared with FEM models without hardening. It is found that for elastic-plastic contact, hardening behavior is very important and must be considered. The material with high hardening will lead to a larger maximum pressure and a smaller plastic region.

Acknowledgment

The authors would like to thank the valuable suggestions from Professors J. Wang and B. Moran at Northwestern University. This work was supported through the Center for Surface Engineering and Tribology, an NSF I/UCRC.

Appendix

An EPC code is written using FORTRAN language. The dominating steps are as follows:

1. Set the grid system. Calculate influence coefficient matrix \mathbf{K} , \mathbf{A} , and \mathbf{D} in Eqs. (11), (25), and (23).
2. Begin the loading loop. $L=L+\Delta L$
3. Set the initial residual displacement increment.
4. Begin the elastic-plastic contact loop.
5. Elastic contact calculation. Obtain p , σ_{pressure} , and $\delta\sigma_{\text{pressure}}$.
6. Calculate initial plastic strain increment.
7. Begin the plastic strain loop. Calculate residual stress increment. $\delta\sigma_r(M)=\sum_{n=1}^{N_v}\mathbf{A}(M,C)\delta\epsilon^n(C)$
8. Calculate plastic strain increment. $\delta\epsilon^p=f(\sigma_{\text{pressure}},\sigma_r,\delta\sigma_{\text{pressure}},\delta\sigma_r)$
9. Calculate the current error of the plastic strain loop $\Delta\delta\epsilon^p$.
10. If $\Delta\delta\epsilon^p/\max|\delta\epsilon^p|>eps_1$, then $\delta\epsilon^p=\delta\epsilon^p+\lambda_1\Delta\delta\epsilon^p$, go to step 7; otherwise, stop plastic strain loop.
11. Calculate the increment of residual displacement. $\delta u_{3(r)}(A)=\sum_{n=1}^{N_v}\mathbf{D}(n)\delta\epsilon^n(n)$
12. Calculate the current error of elastic-plastic loop $\Delta\delta u_{3(r)}$.
13. If $\Delta\delta u_{3(r)}/\max|\delta u_{3(r)}|>eps_2$, then $\delta u_{3(r)}=\delta u_{3(r)}+\lambda_2\Delta\delta u_{3(r)}$, go to step 4; otherwise, stop elastic-plastic loop.
14. If $L<L_{\text{max}}$, go to step 2; otherwise, stop loading loop.
15. Stop the program.

References

- [1] Greenwood, J. A., and Williamson, J. B. P., 1966, "Contact of Nominally Flat Surfaces," *Proc. R. Soc. London, Ser. A*, **295**, pp. 300–319.
- [2] Tsukizoe, T., and Hisakado, T., 1965, "On Mechanism of Contact between Metal Surfaces—Penetrating Depth and Average Clearance," *J. Basic Eng.*, **87**(3), pp. 666–674.
- [3] Tsukizoe, T., and Hisakado, T., 1968, "On Mechanism of Contact between Metal Surfaces. 2. Real Area and Number of Contact Points," *Mech. Eng. (Am. Soc. Mech. Eng.)*, **90**(1), p. 73.
- [4] Onions, R. A., and Archard, J. F., 1973, "Contact of Surfaces Having a Random Structure," *J. Phys. D*, **6**(3), pp. 289–304.
- [5] Mikic, B. B., and Roca, R. T., 1974, "Solution to Contact of 2 Rough Spherical Surfaces," *J. Appl. Mech.*, **41**(3), pp. 801–803.
- [6] Bush, A. W., Gibson, R. D., and Thomas, T. R., 1975, "Elastic Contact of a Rough Surface," *Wear*, **35**(1), pp. 87–111.

- [7] Bush, A. W., Gibson, R. D., and Keogh, G. P., 1976, "Limit of Elastic Deformation in Contact of Rough Surfaces," *Mech. Res. Commun.*, **3**(3), pp. 169–174.
- [8] Bush, A. W., Gibson, R. D., and Keogh, G. P., 1977, "Strongly Anisotropic Rough Surfaces," *ASME J. Lubr. Technol.*, **101**, pp. 15–20.
- [9] Suratkarn, P. T., Pandit, S. M., and Wu, S. M., 1976, "A Stochastic Approach to the Mode of Deformation and Contact Between Rough Surfaces," *Wear*, **39**, pp. 239–250.
- [10] Zhao, Y. W., Maietta, D. M., and Chang, L., 2000, "An Asperity Microcontact Model Incorporating the Transition From Elastic Deformation to Fully Plastic Flow," *J. Tribol.*, **122**(1), pp. 86–93.
- [11] Liu, Z. Q., Neville, A., and Reuben, R. L., 2000, "An Analytical Solution for Elastic and Elastic-Plastic Contact Models," *Tribol. Trans.*, **43**(4), pp. 627–634.
- [12] Chang, W. R., Etsion, I., and Bogoy, D. B., 1987, "An Elastic-Plastic Model for the Contact of Rough Surfaces," *J. Tribol.*, **109**(2), pp. 257–263.
- [13] Gupta, V., Hahn, G. T., Bastias, P. C., and Rubin, C. A., 1995, "Contribution of Surface Irregularities to Rolling Contact Plasticity in Bearing Steels," *ASME J. Tribol.*, **117**, pp. 660–666.
- [14] Liu, G., et al., 2001, "Elasto-Plastic Contact of Rough Surfaces," *Tribol. Trans.*, **44**(3), pp. 437–443.
- [15] Kogut, L., and Etsion, I., 2002, "Elastic-Plastic Contact Analysis of a Sphere and a Rigid Flat," *J. Clim.*, **69**(5), pp. 657–662.
- [16] Mesarovic, S. D., and Fleck, N. A., 1999, "Spherical Indentation of Elastic-Plastic Solids," *Proc. R. Soc. London, Ser. A*, **455**(1987), pp. 2707–2728.
- [17] Komvopoulos, K., and Choi, D. H., 1992, "Elastic Finite-Element Analysis of Multiasperity Contacts," *J. Tribol.*, **114**(4), pp. 823–831.
- [18] Love, A. E. H., 1952, *A Treatise on the Mathematical Theory of Elasticity*, Cambridge University Press, Cambridge.
- [19] Poon, C. Y., and Sayles, R. S., 1994, "Numerical Contact Model of a Smooth Ball on an Anisotropic Rough-Surface," *J. Tribol.*, **116**(2), pp. 194–201.
- [20] Lubrecht, A. A. a. L. E., 1991, "A Fast Solution of the Dry Contact Problem and the Associated Subsurface Stress Field, Using Multilevel Techniques," *J. Tribol.*, **113**, pp. 128–132.
- [21] Polonsky, I. A., and Keer, L. M., 1999, "A Numerical Method for Solving Rough Contact Problems Based on the Multi-Level Multi-Summation and Conjugate Gradient Techniques," *Wear*, **231**(2), pp. 206–219.
- [22] Ju, Y., and Farris, T. N., 1996, "Spectral Analysis of Two-Dimensional Contact Problems," *J. Tribol.*, **118**, pp. 320–328.
- [23] Polonsky, I. A., and Keer, L. M., 2000, "A Fast and Accurate Method for Numerical Analysis of Elastic Layered Contacts," *J. Tribol.*, **122**(1), pp. 30–35.
- [24] Liu, S. B., Wang, Q., and Liu, G., 2000, "A Versatile Method of Discrete Convolution and FFT (DC-FFT) for Contact Analyses," *Wear*, **243**(1–2), pp. 101–111.
- [25] Nogi, T., and Kato, T., 1997, "Influence of a Hard Surface Layer on the Limit of Elastic Contact. 1. Analysis Using a Real Surface Model," *J. Tribol.*, **119**(3), pp. 493–500.
- [26] Stanley, H. M., and Kato, T., 1997, "An FFT-Based Method for Rough Surface Contact," *J. Tribol.*, **119**(3), pp. 481–485.
- [27] Jacq, C., et al., 2002, "Development of a Three-Dimensional Semi-Analytical Elastic-Plastic Contact Code," *J. Tribol.*, **124**(4), pp. 653–667.
- [28] Mayeur, C., Sainsot, P., and Flamand, L., 1995, "A Numerical Elastoplastic Model for Rough Contact," *ASME J. Tribol.*, **117**, pp. 422–429.
- [29] Boussinesq, J., 1885, *Application des Potentials a l'Etude de l'Equilibre et du Mouvement des Solids Elastique*, Gauthier-Villars, Paris.
- [30] Cerruti, V., 1882, Roma, Acc. Lincei, Mem. fis. mat.
- [31] Liu, G., Wang, Q. J., and Lin, C., 1999, "A Survey Of Current Models for Simulating the Contact Between Rough Surfaces," *Tribol. Trans.*, **42**(3), pp. 581–591.
- [32] Johnson, K. L., 1985, *Contact Mechanics*, Cambridge University Press, Cambridge.
- [33] McCormic, G. P., 1983, *Nonlinear Programming: Theory, Algorithms, and Applications*, Wiley, New York.
- [34] Minoux, M., 1986, *Mathematical Programming: Theory and Algorithms*, Wiley-Interscience series in discrete mathematics and optimization, Wiley, Chichester.
- [35] Pshenichny, B. N. a. Y. M. D., 1975, *Numerical Methods in Optimization Problem*, Nauka, Moscow.
- [36] Kalker, J. J., 1986, "Numerical Calculation of the Elastic Field in a Half-Space," *Comm. Appl. Numer. Methods*, **2**, pp. 401–410.
- [37] Stoer, J. a. R. B., 1980, *Introduction to Numerical Analysis*, Springer, New York.
- [38] Liu, S. B., and Wang, Q., 2002, "Studying Contact Stress Fields Caused by Surface Traction With a Discrete Convolution and Fast Fourier Transform Algorithm," *J. Tribol.*, **124**(1), pp. 36–45.
- [39] Brebbia, L. C., 1980, "The Boundary Element Method for Engineers," Pentech, London.
- [40] Chiu, Y. P., 1977, "Stress-Field Due to Initial Strains in a Cuboid Surrounded by an Infinite Elastic Space," *J. Appl. Mech.*, **44**(4), pp. 587–590.
- [41] Chiu, Y. P., 1978, "Stress-Field and Surface Deformation in a Half Space with a Cuboidal Zone in Which Initial Strains Are Uniform," *J. Appl. Mech.*, **45**(2), pp. 302–306.